Provided for non-commercial research and education use.
Not for reproduction, distribution or commercial use.

This article was published in an Elsevier journal. The attached copy is furnished to the author for non-commercial research and education use, including for instruction at the author's institution, sharing with colleagues and providing to institution administration.

Other uses, including reproduction and distribution, or selling or licensing copies, or posting to personal, institutional or third party websites are prohibited.

In most cases authors are permitted to post their version of the article (e.g. in Word or Tex form) to their personal website or institutional repository. Authors requiring further information regarding Elsevier's archiving and manuscript policies are encouraged to visit:

http://www.elsevier.com/copyright

Author's personal copy

Available online at www.sciencedirect.com
ScienceDirect
International Journal of Fatigue 29 (2007) 1812–1819
International Journal of Fatigue
www.elsevier.com/locate/ijfatigue

A neutron-diffraction study of the low-cycle fatigue behavior of HASTELLOY® C-22HS™ alloy

E.-Wen Huang [a,*], Bjørn Clausen [b], Yandong Wang [a,c], Hahn Choo [a], Peter K. Liaw [a], Michael L. Benson [a], Lee M. Pike [d], Dwaine L. Klarstrom [d]

[a] *Materials Science and Engineering Department, University of Tennessee, 434 Dougherty Hall, Knoxville, Tennessee 37996, USA*
[b] *Los Alamos Neutron Science Center, Los Alamos National Laboratory, USA*
[c] *School of Materials and Metallurgy, Northeastern University, China*
[d] *Haynes International, Inc., Kokomo, IN 46904-9013, USA*

Available online 12 February 2007

Abstract

The HASTELLOY® C-22HS™ alloy is a face-centered cubic (fcc), nickel-based, corrosion-resistant superalloy. In the present study, the low-cycle-fatigue behaviors of the alloy were examined by in situ neutron diffraction at room temperature. The fatigue parameters included a total strain range of $\Delta\varepsilon = 2\%$ and a strain ratio of $R = -1$ ($R = \varepsilon_{min}/\varepsilon_{max}$, where ε_{min} and ε_{max} are the applied minimum and maximum strains, respectively). The effect of cyclic deformation on the lattice strains was studied as a function of cyclic straining. The cyclic hardening and softening behaviors during fatigue is discussed in light of the relationship between the peak widths and lattice strains.
© 2007 Elsevier Ltd. All rights reserved.

Keywords: Low-cycle fatigue; In situ neutron diffraction; Cyclic hardening; Cyclic softening

1. Introduction

Fatigue studies are essential for the applications of conventional and advanced materials subjected to cyclic loading [1,2]. The fatigue behaviors of corrosion-resistant superalloys are important because these alloys are extensively used in harsh environments and expected to withstand thermo-mechanical cyclic loading [3,4]. The present work describes an experimental investigation of the fatigue deformation in the mill-annealed, corrosion-resistant, Ni-based C-22HS alloy using in situ neutron-diffraction measurements. It is an alloy intended to be used in aqueous corrosion applications where high strength is required. The current measurements conducted at room temperature provide the baseline information for future experiments in highly-corrosive environments. The neutron-diffraction experiment is an excellent tool to study the fatigue behavior [5–9] because neutrons have a good penetration capacity [10], which facilitates the study of the bulk properties from the statistical average of the microscopic behavior. The diffraction data were collected from a single specimen at different fatigue cycles. The aim of the present research is to identify the cyclic hardening and softening characteristics during low-cycle fatigue and to illustrate how the neutron-diffraction results could be used to understand the cyclic plasticity.

2. Testing materials and experiments

Corrosion-resistant nickel-based superalloys are widely used in engineering applications because of their excellent resistance to a wide variety of corrosive environments. The C-22HS alloy [11,12] is one of the commercial alloys developed by Haynes International, Inc for use in the chemical process industry. The composition is listed in Table 1, and American Society for Testing and Materials Standards (ASTM) grain-size number is 4, which corre-

* Corresponding author. Tel.: +1 8659745413; fax: +1 8659744115.
E-mail address: ehuang1@utk.edu (E.-Wen Huang).

0142-1123/$ - see front matter © 2007 Elsevier Ltd. All rights reserved.
doi:10.1016/j.ijfatigue.2007.01.025

Author's personal copy

sponds to an average grain diameter of about 90 μm. After a hot-rolling process, the alloy was mill annealed at 1080 °C. In the mill-annealed condition, the alloy is in a face-centered-cubic (fcc) structure with scattered carbides. A transmission-electron-microscopy (TEM) study demonstrated that there were no long-range-order (LRO) domains found in the annealed microstructure [6], and X-ray pole-figure measurements showed that no strong texture exists in the alloy investigated.

The in situ low-cycle-fatigue test was performed using the Spectrometer for MAterials Research at Temperature and Stress (SMARTS) at the Los Alamos Neutron Science Center (LANSCE) [13]. The alloy was measured by the neutrons, and these neutron-diffraction patterns were refined by the general structure analysis system (GSAS) software package [14] using Rietveld analyses [15]. Rietveld analyses refine the whole diffraction pattern based on the crystallographic structure, including the lattice parameters. The fitted results of the undeformed alloy in the mill-annealed condition are shown in Fig. 1. Only the diffraction peaks from the matrix (fcc crystal structure) are observed as the volume fraction of carbides is too small to register in the diffraction pattern. Only the fcc diffraction peaks from the matrix were monitored during the following in situ fatigue experiments.

The in situ neutron-diffraction fatigue test was conducted at room temperature, where the minimum strain (ε_{min}) and the maximum strain (ε_{max}) are 1% and −1%, respectively. For the low-cycle-fatigue sample was aligned 45° to the incident neutron beam with two detector banks fixed at $2\theta = \pm 90°$, and the gauge volume was 120 mm^3. Hence, one detector collected the diffraction data along the loading direction (the axial data), and the other collected the diffraction data normal to the loading direction (the transverse data). This scattering geometry followed the method established in the previous in situ loading neutron-diffraction research [16–22]. The diffraction data was collected at different cycles during the fatigue experiment: 1, 4, 8, 12, 30, 50, 100, 250, 500, 1000, 1250, and 1500 cycles. The frequency of the loading cycle was 0.5 Hz.

The cyclic-loading sequence is shown in Fig. 2. Point 0 is the origin point, and then the specimen was loaded to reach a maximum macro strain of 1% at Point 1. At Point 2, the sample was unloaded to reach 0 MPa as an external-stress-free status. At Point 3, the sample was compressed to a macro strain of 0%. At Point 4, the sample was compressed to reach a macro strain of −1%. At Point 5, the sample was unloaded from compression to 0 MPa. At Point 6, the sample was loaded to a macro strain of 0%. Finally, at Point 7 we loaded the specimen to reach a maximum macro strain of 1% again, which is the same as the Point 1 to compare the change made by one cycle. The neutron measurements were performed at these 7 points for each cycle listed above.

Other cyclic loading to failure experiments under the same experimental conditions have been conducted on the alloy to examine its lifetime. The fracture surface of the cyclic failure specimen has been studied by the scanning-electron-microscopy (SEM).

Table 1
The composition of the HASTELLOY® C-22 HS™ alloy [6]

HASTELLOY C-22 HS	Ni	Cr	Mo	W	Fe	C
Weight percentage	61	21	17	1[a]	2[a]	0.01[a]

[a] Maximum.

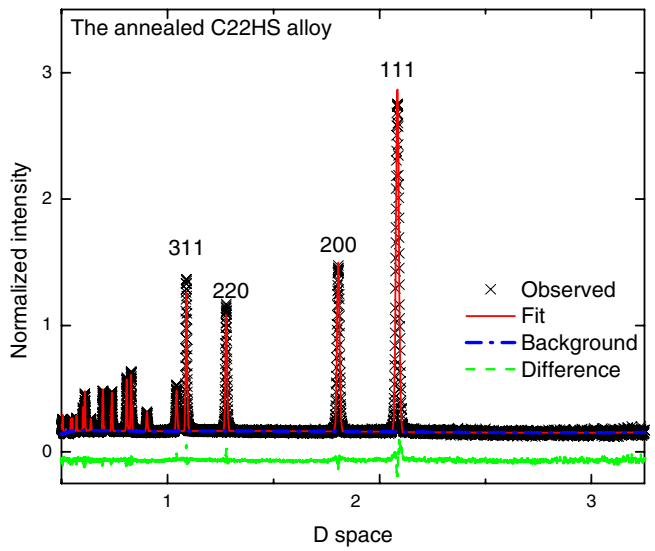

Fig. 1. The Rietveld fitting of the neutron-diffraction patterns in the axial direction demonstrating that the undeformed alloy is in a fcc structure. The *D*-spacing is 2.084A for 111, 1.805A for 200, 1.276A for 220, and 1.088A for 311.

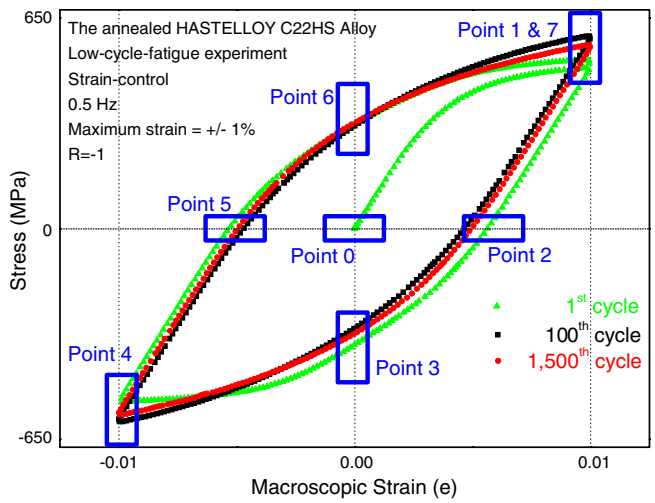

Fig. 2. The low-cycle-fatigue hysteresis loop of the annealed C22HS alloy. The loop of the green solid triangles is the first cycle. The cyclic hardening is clearly visible at Point 1 during the first cycle. The loop of the 100th is in black and the 1500th is in red. From the comparison of the applied stress at Point 1, it clearly shows that the alloy was hardened at 100th cycle and then softened at 1500th cycle. (For interpretation of the references to colour in this figure legend, the reader is referred to the web version of this article.)

Author's personal copy

3. Results

The results of a low-cycle-fatigue failure experiment are described first. The lifetime of this alloy is about 10,000 cycles. A SEM examination of the other failed specimen generated by this low-cycle-fatigue experiment is shown in Fig. 3a. The fracture surface is flatter than the monotonic tensile-failure specimen. The regions marked as A in Fig. 3a are the crack-initiation regions of this low-cycle-fatigue experiment. The striations, on the fracture surface (region A) as revealed in Fig. 3b, map instantaneous positions of the initiating crack tip during fatigue-crack propagation. The arrow in Fig. 3b marks the main direction of crack growth. The deformation associated with these tension and compression sequences of the crack produced the striated appearance. The regions, marked B in Fig. 3a, are the fast-fracture regimes of this low-cycle-fatigue experiment. Region B consists of hollow dimples on the surface as shown in Fig. 3c. The parabola-shaped features on the fracture surface indicate that the cavities are elongated in the direction of the shear bands.

The following observations and discussion will focus on the phenomena at the 7 points within the 1500th fatigue cycle. Fig. 4 shows the macro stress as a function of the number of cycles from the 1st to 1500th cycle with in situ neutron measurements. At Points 1, 3, 4, and 6, the sample was held in strain control at 1%, 0%, −1%, and 0%, respectively. At Points 2 and 5, the sample was held at zero stress. Hence, there is no variation in the true stress as a function of cycles for Points 2 and 5. It is evident that the stresses at Points 1 and 4 (maximum positive and negative strains, respectively) are symmetric, and likewise so are the stresses at Points 3 and 6 (zero strain). The stress levels at Points 1 and 4 increase as a function of fatigue cycles until about 50 cycles after which they decrease and level out at 547 MPa and −523 MPa, respectively, which are about 30% higher than for the initial cycle. The stress levels at Points 3 and 6 also increase up to about 30 cycles, but then decrease

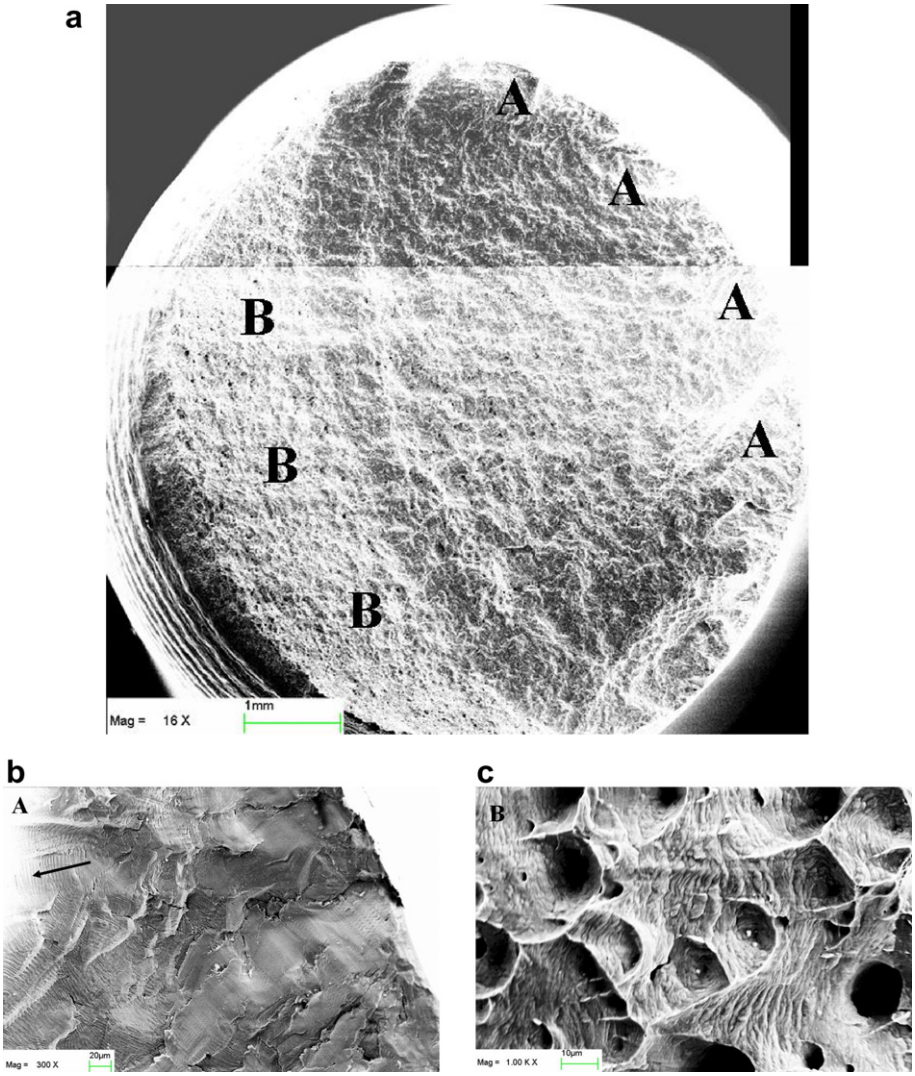

Fig. 3. The alloy was cyclically deformed until failure. (a) The overview of the fatigue failure specimen where A is the initial stage and B is the final stages with dimples, (b) the striations indicate the crack propagation direction, and the dimples are shown in (c).

Author's personal copy

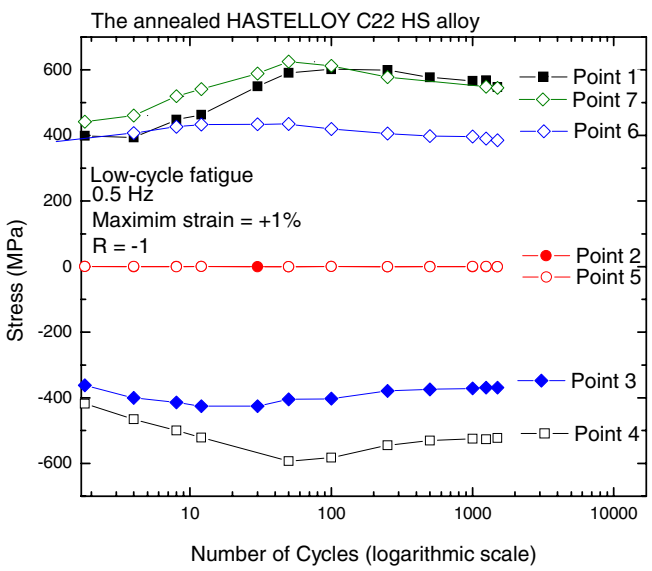

Fig. 4. The alloy was cyclically deformed up to 1500 fatigue cycles. The stress at each point of the hysteresis loop (Fig. 2) is shown as a function of the fatigue cycle. Note the error bar that is less than 0.5 MPa, i.e., much less than the symbol size in the plot.

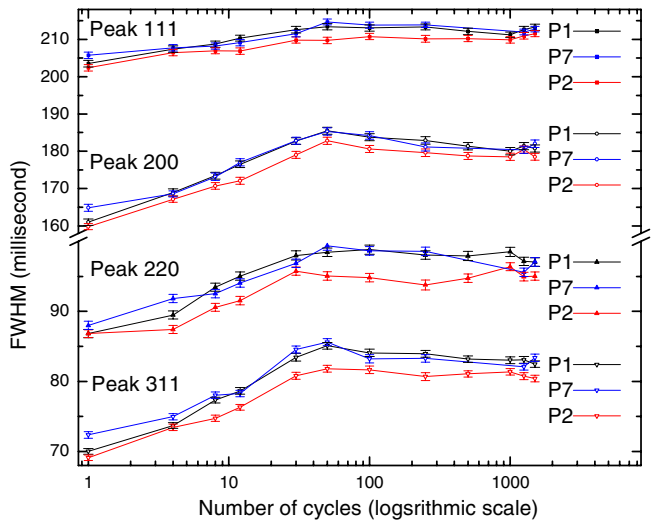

Fig. 5. The alloy was cyclically deformed up to 1500 fatigue cycles. The peak-widths evolution of peaks 111 (solid square), 200 (hollow circle), 220 (solid upward triangle) and 311 (hollow downward triangle) at Points 1 (in black), Point 2 (in red) and Point 7 (in blue) are shown as a function of the fatigue cycle. The unit is the millisecond of the time-of-flight as shown in Fig. 4. (For interpretation of the references to colour in this figure legend, the reader is referred to the web version of this article.)

down to approximately the same level around 400 MPa as for the initial cycle. It is interesting to compare the different stresses made by single cyclic loading measured at Points 1 and 7, where the strains are the same. Before the 100th cycle, the stresses at Point 7 are greater than that of Point 1. They increase about 11% at 1st cycle, 17%, 16%, 7%, 6%, and 2% for the following 4th, 8th, 12th, 30th, 50th, and 100th cycle, respectively. However, after 100th cycle, the stresses decrease 3% for 1250th and 0.4 for 1500th cycle.

3.1. Peak widths as a function of the fatigue cycles

The neutron-diffraction peak widths are characterized by the full-width at half-maximum (FWHM) for the Gaussian part of the peak profile function. Here we report the peak-widths along the loading direction for Points 1 (the strain level at 1%), 2 (without the applied stress) and 7 (the strain level at 1%) in Fig. 5. The importance of the neutron measurements at numerous Points is to compare the sources of the peak-width broadening because the peak broadening varies with different effects correlating to the different stress and strain levels. The unit of the full width at half maximum (FWHM) peak widths is in milliseconds of time-of-flight. The general trends observed for the peak-width evolution are about the same for the 111, 200, 220, and 311 peaks at all Points. The largest variation of peak broadening is seen for Point 1, where the deformation is controlled at the maximum tensile strain of 1%. A 25% increase at Point 1 in peak 311 is observed at 50 cycles, and then continuously decreases slightly to the 1500th cycle at a value about 17% higher than the initial value. All the peaks broadened at Points 1, 2, and 7 up to about 50 fatigue cycles. These evolutions are similar to the stress evolutions as shown in Fig. 4. Within one cycle, the peak-widths of Point 1 (maximum strain) are typically greater than those of Point 2 (with no applied stress). However, it is not always greater than the peak-widths measured at Point 7 (maximum strain). To have a closer look of the peak width evolutions within one fatigue cycle, we plot the peak width as a function of points for 1st, 100th, and 1000th cycles. Peak 111 is plotted in Fig. 6a, 200 in (b), 220 in (c), and 311 in (d). For all four peaks, the peaks are broadened significantly within one cycle at the 1st cycle, but not in the 100th and 1000th cycles. On the contrast, peak widths of 220 and 311 decrease after the 1000th cycle. More details are discussed later.

3.2. Lattice strains as a function of the number of cycles

The lattice strains, ε_{hkl}, are calculated by the changes in the d-spacing, d_{hkl}, at different fatigue cycles with respect to that of the reference d-spacing, d^0_{hkl}, as shown in Eq. (1) [14]. The reference lattice spacing, d^0_{hkl}, is determined from the measured lattice spacing before the cyclic loadings.

$$\varepsilon_{hkl} = \frac{d_{hkl} - d^0_{hkl}}{d^0_{hkl}} \tag{1}$$

We observed the lattice strains of 111, 200, 220, and 311 in the unit of micro-strain (με). Fig. 7 shows the lattice strains of 111, 200, 220, and 311 at Point 1 in black and Point 2 in red. The lattice strains measured at Point 1 and 7 are at 1% strain level, where the specimen exceeded the plastic deformation. There was no applied stress while measuring the lattice strains at Point 2, and thus the lattice strains measured at Point 2 are the residual strains. It is interesting to note that although the engineering strain is controlled to be 1% at Points 1 and 7, the lattice strains

Author's personal copy

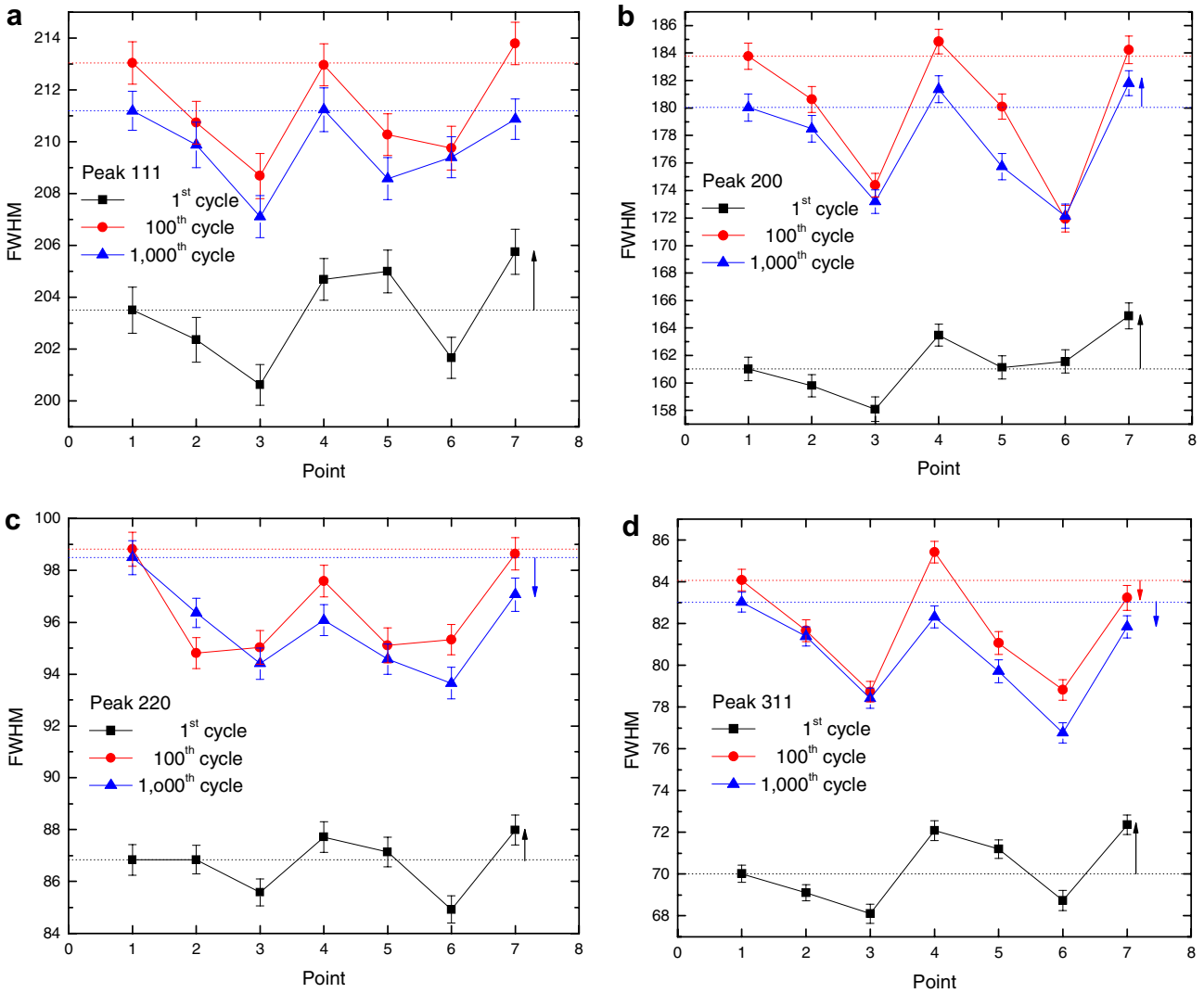

Fig. 6. Peak widths of cycles 1st (black), 100th (red) and 1000th (blue) are plotted as a function of Points for (a) 111, (b) 200, (c) 220, and (d) 311 peaks. The dash lines indicate the peak width of the Point 1 of the each cycle. (For interpretation of the references to colour in this figure legend, the reader is referred to the web version of this article.)

are not constant, as shown in Fig. 7. This trend indicates that the intergranular stress indeed develops during the cyclic deformation. Comparing to Fig. 4, the lattice strain at Point 1 evolve accordingly with the stress. In Fig. 7, all the lattice strains at Point 1 increase and then decrease in the same manner as the stress found in Fig. 4. At Point 2 the applied stress was controlled to be 0 MPa and thus the neutron-diffraction data demonstrates the residual lattice strains at Point 2 in Fig. 7. The evolutions of lattice strains between Points 1 and 7, correlate to the evolution of the stress, where before 100th cycle, the lattice strains at Point 7 are greater than that of Point 1, but become smaller when fatigue cycles are greater than 100.

4. Discussion

Fig. 8 is the plot of the applied stress vs. the lattice strains of 111, 200, 220, and 311 at Point 1. The lattice strains increased during cyclic hardening and decreased during cyclic softening as noted on the Fig. 8. During the hardening cycles, as the fatigue cycles increased, the elastic strains increased. The inflection region is found at about the 100th cycles. After that, the elastic strains decreased as the fatigue cycles increased within the cyclic-softening region. According to Hook's law, the elastic strains response to the applied stress, the linear relationships are found in all the diffraction peaks at the Points 1 accordingly. For more details, all four diffraction peaks keep the linear relationship very well where the 1% strain was controlled. However, peaks 200 and 220 deviate from the linear relationship at the softening cycles. These deviations indicate the development of the intergranular strains as previously investigated in detail [3].

Moreover, it is interesting to compare the level of the plastic strain stored in the material with the diffraction-elastic strains and the bulk energy. The calculations of

Author's personal copy

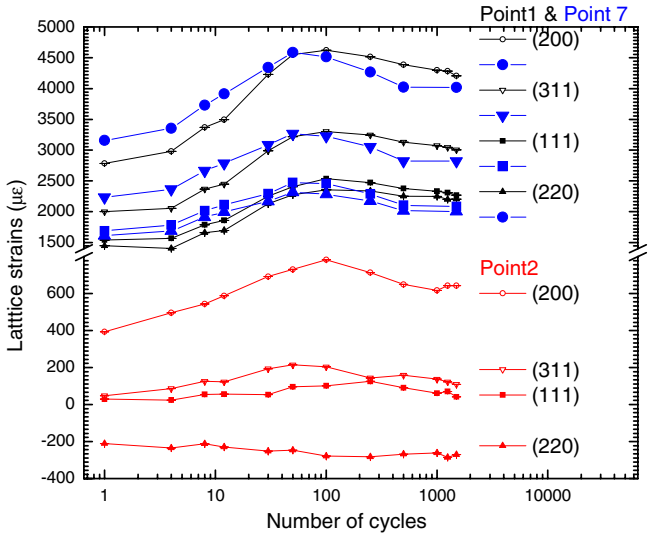

Fig. 7. The evolutions of the diffraction lattice strains of peak 1 1 1 (square), 2 0 0 (circle), 2 2 0 (upward triangle) and 3 1 1 (downward triangle) are plotted as a function of fatigue cycles at Pont 1 (black), Point 2 (red) and Point 7 (blue). The error bars are on the order of 20 με. (For interpretation of the references to colour in this figure legend, the reader is referred to the web version of this article.)

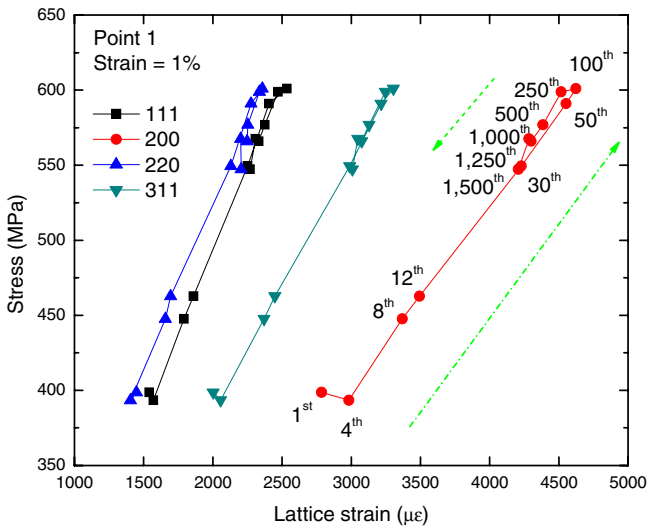

Fig. 8. The stress-lattice strain plot. Peaks 1 1 1 (square) and 3 1 1(downward triangle) keep the linearity through the hardening cycles and softening cycles. Peaks 2 0 0 (circle) and 2 2 0 (upward triangle) stay in good linearity from the 4th to 100th cycle and start to deviate since 100th cycle. Note the error bar that is less than 20 με, i.e., much less than the symbol size in the plot.

the strain energy absorbed by the material during the fatigue cycles are listed below. The total energy (U_{total}) equals the integrated area under the load–deformation curve as the tensile stress (s) multiplied by the strain (e) in Eq. (2). For the diffraction elastic part, the elastic energy (U_{hkl}) stored in each hkl grain depends on its hkl-modulii (E_{hkl}) which was measured via an in situ neutron, monotonic tension experiment. The hkl elastic energy is calculated by Eq. (3) varies slightly for the reflections, but all show the same general variation.

$$U_{\text{total}} = \int_{e=0}^{e=1\%} s * e_{\text{bulk}} \tag{2}$$

$$U_{hkl} = \frac{e_{hkl}^2 * E_{hkl}}{2} \tag{3}$$

The change of energy is calculated by retrieving the data from Point 1. The evolution of U_{total} is examined from the hysteresis loop as shown in Fig. 2, and U_{hkl} can be estimated from the Fig. 7. Since U_{total} is proportional to the integrated area. Because the hkl-modulii stays constant, as the linearity of the lattice-strain vs. stress shown in Fig. 8, the change of U_{hkl} is proportion to the square of the lattice strain. U_{total} and U_{hkl} follow the same trend as the cyclic hardening and softening shown in Fig. 4. The change of the U_{hkl} is different than that of U_{total}, which indicates that the transition of the plastic deformation involves as the number of the fatigue cycle. To further understand the phenomena, it is necessary to consider the information on the stored-energy retrieved from the peak-shape profiles.

The intrinsic peak-shape broadening of neutron-diffraction peaks can have several origins, which include the stored energy, dislocation configurations, and hkl-dependent contrast of dislocations. Hutchings et al. [21], Barabash and co-workers [23], and Šittner et al. [24] reported that the evolution of the peak width is due to the change of the number of scattering sites. Jakobsen et al. [25] also finds that these changes of the peak-width come from the change of the substructure of the grains. They reported the relationships of the diffraction patterns with the microstructures that distinguish the intergranular and intragranular strains. The intergranular strains are analogous to that of the grain structure and correspond to the type II stresses, which arise among the different grains at various orientations [21]. The intragranular strains depend on the type III stresses from the grain subdivision, and therefore, vary within a grain [21]. The increase of the peak width observed in this study is mainly due to two reasons: first, the intergranular strains come from the elastic and plastic anisotropy, and secondly the intragranular strains due to dislocation density. To compare these two reasons, a comparison of peak widths within one fatigue cycle is discussed below. In Fig. 5, since peak widths vary as a function of cycles more than that of different Points, the accumulated dislocations during texture development could occur. In Fig. 6a–d, peaks widths of Points 1, 4, and 7 are typically highest due to the applied stress. The peak widths are lower at the unloaded Points 2 and 5 as there is no applied stress. However, at these unloaded Points, there are still both inter and intragranular strains that cause peak widths change compared to the undeformed specimen as shown in Fig. 5. All these peak widths evolve in a similar pattern as a function of the fatigue cycles due to the change of the intragranular strains. The residual-lattice strain evolu-

Author's personal copy

tions, measured at Point 2, as shown in Fig. 7, demonstrate how the residual stress changes as a function of the fatigue cycles. The peak-width evolutions of residual status (Fig. 5) correlate to the applied stress (Fig. 4) since the main peak broadening is caused by the dislocation density changes, developments and their arrangements. Because dislocations can produce severe short-range elastic strains, the peak-width could infer the dislocation density unless the dislocations are clustered into cells or boundaries [21]. The difference peak widths at Points 1 and 2 are due to the intergranular strains caused by the applied stress (elastic anisotropy).

Above all, during cyclic hardening, the internal strains/stress increased might vary with the increase of the dislocation density. The decrease of the peak widths indicates that the dislocations might rearrange, which could be due to dislocations clustering into cells walls or grain boundaries [26–28]. The stress as a function of fatigue cycles in Fig. 4 agrees with the evolution of the peak-width in Fig. 5, which shows the effect of the dislocation density and the rearrangement as the cyclically loadings. Based on the above discussion, we assume that the fatigue damage occurs when strains are accumulated and produce dislocations during the low-cycle fatigue experiments. The studies of diffraction patterns have brought a basic understanding to the fatigue process. The nature and the stability of the dislocation substructure of the materials could contribute to this cyclic hardening and softening phenomena.

5. Summary

In situ neutron-diffraction study of the low-cycle fatigue with $\Delta\varepsilon = 2\%$ and $R = -1$ showed a cyclic hardening behavior followed by cyclic softening. The peak-width evolution of neutron-diffraction profiles can reflect the cyclic hardening and softening behaviors, which indicates that, the increase in the dislocation density and the rearrangement in dislocations, respectively, and, hence, change the lattice strains. The cause and the effect of the cyclically hardening and softening behaviors were monitored by the peak widths and the lattice strains simultaneously. This in situ neutron study could be applied as the nondestructive technique to examine the low-cycle-fatigue behaviors.

Acknowledgements

This research is supported by the National Science Foundation (NSF), International Materials Institutes (IMI) Program (DMR-0231320). Dr. Carmen Huber is the Director of the IMI program. The Lujan Neutron Scattering Center at LANSCE is funded by the Department of Energy's Office of Basic Energy Science. The Los Alamos National Laboratory (LANL) is operated by the Los Alamos National Security LLC under the DOE Contract DE-AC52-06NA25396. We appreciate the discussions with Dr. Donald W. Brown and Dr. Tarik Saleh at LANL.

References

[1] Forró L. Display of flexibility. Nature 2006;441:414–5.
[2] Junquera J, Ghosez P. Critical thickness for ferroelctricity in perovskite ultrathin films. Nature 2003;422:506–9.
[3] Wang YD, Tian H, Stoica AD, Wang XL, Liaw PK, Richardson JW. The development of grain-orientation-dependent residual stresses in a cyclically deformed alloy. Nat Mater 2003;2:101–6.
[4] Sato J, Omori T, Oikawa K, Ohnuma I, Kainuma R, Ishida K. Cobalt-base high-temperature alloys. Science 2006;312:90–1.
[5] Loge RE, Turkmen HS, Miller MP, Rogge R, Dawson PR. Influence of modeling variables on the distribution of lattice strains in a deformed polycrystal, with reference to neutron diffraction experiments. Model Simul Mater Sci Eng 2004;12:633–63.
[6] Turkmen HS, Loge RE, Dawson PR, Miller MP. On the mechanical behaviour of AA 7075-T6 during cyclic loading. Int J Fatigue 2003;25:267–81.
[7] Webster GA, Ezeilo AN. Residual stress distributions and their influence on fatigue lifetimes. Int J Fatigue 2001;23:5375–83.
[8] Cheng X, Fisher JW, Prask HJ, Gnäupel-Herold T, Yen BT, Roy S. Residual stress modification by post-weld treatment and its beneficial effect on fatigue strength of welded structures. Int J Fatigue 2003;25:1259–69.
[9] Sun Y, Choo H, Liaw PK, Lu Y, Yang B, Brown DW, Bourke MAM. Neutron diffraction studies on lattice strain evolution around a crack-tip during tensile loading and unloading cycles. Scripta Mater 2005;53:971–5.
[10] Pynn R. Neutron scattering a primer. Los Alamos Science; 1990. pp. 1–31.
[11] Pike LM and Klarstrom DL. A new corrosion-resistant Ni–Cr–Mo alloy with high strength, 2004 Corrosion 2004, Paper No. 04239, NACE International, Houston, Texas.
[12] Lu YL, Pike LM, Brooks CR, Liaw PK, Klarstrom DL. Strengthening domains in a Ni–21-Cr–17Mo alloy. Scripta Mater 2007;56:121–4.
[13] Bourke MAM, Dunand DC, Ustundag E. SMARTS – a spectrometer for strain measurement in engineering materials. Appl Phys A 2002;74:1707–9.
[14] Von Dreele RB, Jorgensen JD, Windsor CG. Rietveld refinement with spallation neutron powder diffraction data. J Appl Cryst 1982;15:581–9.
[15] Rietveld HM. Line profiles of neutron powder-diffraction peaks for structure refinement. Acta Cryst 1967;22:151.
[16] Brown DW, Bourke MAM, Clausen B, Holden TM, Tome CN, Varma R. A neutron diffraction and modeling study of uniaxial deformation in polycrystalline beryllium. Metall Mater Trans A 2003;34(A):1439–50.
[17] Clausen B, Lorentzen T, Bourke MAM, Daymond MR. Lattice strain evolution during uniaxial tensile loading of stainless steel. Mater Sci Eng A 1999;259:17–24.
[18] Lorentzen T, Daymond MR, Clausen B, Tome CN. Lattice strain evolution during cyclic loading of stainless steel. Acta Mater 2002;50:1627–38.
[19] Daymond MR, Withers PJ. A new stroboscopic neutron diffraction method for monitoring materials subjected to cyclic loads: thermal cycling of metal matrix composites. Scripta Mater 1996;35(6):717–20.
[20] Korsunsky AM, James KE, Daymond MR. Intergranular stresses in polycrystalline fatigue: diffraction measurement and self-consistent modeling. Eng Fract Mech 2004;71:805–12.
[21] Hutchings MT, Withers PJ, Holden TM, Lorentzen T. Introduction to the characterization of residual stress by neutron diffraction. CRC press, Taylor & Francis group; 2005.
[22] Quinta da Fonseca J, Oliver EC, Bate PS, Withers PJ. Evolution of intergranular stresses during in situ straining of IF steel with different grain sizes. Mater Sci Eng A 2006;437:26–32.

Author's personal copy

[23] Sun Y, Barabash R, Choo H, Liaw PK, Lu YL, Brown DW, Ice G. Evaluation of the dislocation arrangement near the crack tip region of 316 LN stainless steel by neutron and X-ray diffraction. In: America Conference on Neutron Scattering, St. Charles, Illinois, USA; 2006 [June 18–22].

[24] Šittner P, Luka's P, Neov D, Daymond MR, Nova'k V, Swallowe GM. Stress-induced martensitic transformation in Cu–Al–Zn–Mn polycrystalline investigated by two in situ neutron diffraction techniques. Mater Sci Eng A 2002;324:225–34.

[25] Jakobsen B, Poulsen HF, Lienert U, Almer J, Shastri SD, Sórensen HO, Gundlach C, Pantleon W. Formation and subdivision of deformation structures during plastic deformation. Science 2006;312:889–92.

[26] Laird C. Mechanisms and theories of fatigue, fatigue and microstructure. Metals Park, Ohio: American society for metals; 1979. p. 149–203.

[27] Mughrabi H. Dislocation wall and cell structures and long-range internal stress in deformed metal crystal. Acta Metall. 1983;31:1367–78.

[28] Vasudeven AK, Sadananda K, Louat N. A review of crack closure, fatigue crack threshold related phenomena. Mater Sci Eng A 1994;A188:1–22.